IOP Publishing Phys. Med. Biol. 65 (2020) 035009 (10pp) https://doi.org/10.1088/1361-6560/ab6577

Physics in Medicine & Biology

IPEM Institute of Physics and Engineering in Medicine

PAPER

Count rate capabilities of polycrystalline silicon photon counting detectors for CBCT applications—a theoretical study

Albert K Liang, Youcef El-Mohri, Qihua Zhao, Martin Koniczek and Larry E Antonuk[1,2]

Department of Radiation Oncology, University of Michigan, Ann Arbor, MI 48109, United States of America

[1] Senior author.

[2] Author to whom any correspondence should be addressed.

E-mail: antonuk@umich.edu

RECEIVED
21 August 2019

REVISED
18 December 2019

ACCEPTED FOR PUBLICATION
24 December 2019

PUBLISHED
4 February 2020

Keywords: cone-beam CT, photon counting detectors, pixel circuit, amplifier stage, thin-film transistors, polycrystalline silicon, circuit simulations

Abstract

The signal-to-noise properties of active matrix, flat-panel imagers (AMFPIs) limit the imaging performance of this x-ray imaging technology under conditions of low dose per image frame. This limitation can affect cone-beam computed tomography (CBCT) procedures where an AMFPI is used to acquire hundreds of image frames to form a single volumetric data set. An approach for overcoming this limitation is to replace the energy-integrating pixel circuits of AMFPI arrays with photon counting pixel circuits which examine the energy of each x-ray interaction and count those events whose signals exceed user-defined energy thresholds. A promising material for fabricating the circuits of such photon-counting detectors (PCDs) is polycrystalline silicon (poly-Si)—a semiconductor that facilitates economic manufacture of large area, monolithic arrays of the size presently provided by AMFPIs as well as provides good radiation damage resistance. In this paper, results are reported from a theoretical investigation of the potential for poly-Si PCDs to satisfy the count rate needs, while maintaining good energy resolution, of two CBCT applications—CBCT used for breast imaging and kilo-voltage CBCT used for providing localization information in image guided radiotherapy (referred to as BCT and kV-CBCT, respectively). The study focused on the performance of the critical first component of a PCD pixel circuit, the amplifier, under conditions relevant to the two applications. The study determined that, compared to the average input fluxes associated with BCT and kV-CBCT, a promising amplifier design employing poly-Si thin-film transistors can provide count rates two and four times in excess of those levels, respectively, assuming a dead time loss of 10%. In addition, calculational estimates based on foreseeable poly-Si circuit densities suggest that it should be possible to include sufficient circuitry to support 2 and 3 energy thresholds per pixel, respectively. Finally, prospects for further improvements are discussed.

1. Introduction

The development of active matrix, flat-panel imagers (AMFPIs) starting in the late 1980s led to widespread introduction of this technology to medicine around the turn of the century (Street *et al* 1990, Zhao and Rowlands 1995, Antonuk *et al* 1998). A key component in AMFPIs is the backplane—a substrate upon which a 2D array of imaging pixels has been fabricated, with each pixel incorporating a circuit typically consisting of a single, amorphous silicon thin-film transistor (a-Si:H TFT) connected to a storage capacitor. An x-ray converter positioned over the array takes the form of either a photoconductor (such as amorphous selenium [a-Se] electrically coupled to the pixel storage capacitors) or a scintillator (such as CsI:Tl or Gd_2O_2S:Tb optically coupled to a-Si:H photodiodes that act as storage capacitors). The many advantages offered by AMFPIs (including affordable, large area, monolithic detectors up to ~43 × 43 cm^2, real-time digital readout, and a high degree of radiation damage resistance) led to their widespread adoption in projection imaging applications including radiography, fluoroscopy and mammography. Moreover, the fast image acquisition offered by AMFPIs

(along with developments in x-ray sources and image reconstruction algorithms) facilitated the creation of cone-beam CT (CBCT) systems for volumetric imaging (Jaffray *et al* 2002). While conventional CT scanners remain the gold standard for volumetric imaging in terms of contrast and image acquisition speed, the low cost, small form factor, and low dose associated with CBCT systems led to their successful implementation in applications such as radiation therapy, otolaryngology, neuroradiology, dental maxillofacial, musculoskeletal and breast imaging (Boone *et al* 2001, Jaffray *et al* 2002, Guerrero *et al* 2006, Rumboldt *et al* 2009, Hodez *et al* 2011, Zbijewski *et al* 2011). Moreover, CBCT systems can facilitate more realistic functional imaging such as for weight-bearing lower extremities (Zbijewski *et al* 2011).

Despite their advantages, the imaging performance of AMFPIs is constrained by a relatively large amount of additive electronic noise compared with the average imaging signal generated per interacting x-ray—leading to loss of detective quantum efficiency (DQE) and image quality under conditions of low dose per frame or at high spatial resolutions (Antonuk *et al* 2000, Segui and Zhao 2006). This limitation affects a variety of applications served by AMFPIs including those using CBCT since this volumetric technique involves the acquisition of numerous individual projection images (from several hundred to over a thousand) in order to form the image data set (Sarno *et al* 2015, Abuhaimed *et al* 2018)—in turn requiring that the individual images be acquired at low dose so as to allow the total imaging dose to remain clinically acceptable.

Approaches being examined to address the signal-to-noise limitations of AMFPIs include the introduction of x-ray converter materials offering intrinsically higher gain (such as HgI_2, PbI_2 and PbO) or avalanche gain (with a-Se) (Street *et al* 2002, Zhao *et al* 2005, Oh *et al* 2012, Jiang *et al* 2013, Scheuermann *et al* 2015). Another approach involves replacement of the simple pixel circuits of AMFPI backplanes with circuits that incorporate an amplifier in every pixel—referred to as an active pixel (AP) design. While the possibility of AP imagers fabricated from semiconductor materials that lend themselves to the manufacture of large area, monolithic backplanes is under investigation (Koniczek *et al* 2017), AP imagers based on crystalline silicon (c-Si) semiconductor (referred to as CMOS sensors) have been successfully introduced to a number of medical imaging applications, and have been reported for CBCT breast and musculoskeletal imaging (Shen *et al* 2013, Gazi *et al* 2015, Cao *et al* 2018). However, unlike AMFPIs based on a-Si:H TFTs, CMOS sensors do not provide high resistance to radiation damage. Moreover, since the underlying fabrication technology for c-Si devices does not lend itself to economic manufacture of large area, monolithic devices, imagers are limited in area (currently up to 31×31 cm^2) (Job *et al* 2019) and are typically assembled by tiling many small individual CMOS sensors—adding to their expense.

An alternative approach for overcoming the signal-to-noise limitations of AMFPIs is to replace the energy-integration method used in those systems with photon counting. In energy integration, the signals generated by x-rays interacting in the converter during a given image frame are accumulated in the array pixels prior to readout of that analog signal information by external acquisition electronics. By comparison, in photon counting, considerably more complex pixel circuitry than that employed in AMFPI backplanes is used to record information about individual x-rays in each pixel. In the most basic configuration of the type of device considered in this study, every pixel circuit of a photon-counting detector (PCD) consists of four components: an amplifier, a comparator, a clock generator and a digital counter (Liang *et al* 2016). The signal presented to a pixel from a given interacting x-ray is amplified and compared against a user-defined threshold. For each x-ray event generating a signal whose magnitude is above that threshold, the clock generator increments the tally in the counter by one. The incorporation of additional comparators, clock generators and counters in the pixel circuit facilitates multiple thresholds allowing events to be sorted into multiple energy bins according to the energy deposited in the pixel. Compared to energy-integrating detectors, PCDs offer the advantages of reduced electronic additive noise and Swank noise (Tanguay *et al* 2015). In addition, unlike energy-integrating detectors, PCDs offer the possibility of assigning equal or higher weight to lower energy events which provide inherently better tissue contrast (Taguchi and Iwanczyk 2013). Moreover, the separation of events into multiple energy bins facilitates advanced imaging techniques such as dual-energy imaging, K-edge imaging and material decomposition (Roessl and Proksa 2007, Fredenberg *et al* 2009, Shikhaliev and Fritz 2011, Gutjahr *et al* 2016, Pourmorteza *et al* 2016, 2017, Symons *et al* 2018).

While PCDs with this general type of pixel circuitry have been developed based on c-Si in the form of small, 2D image sensors (Campbell *et al* 1998, Fischer *et al* 2000, Llopart *et al* 2002, Ballabriga *et al* 2011), such c-Si devices are encumbered by the same issues of radiation damage and area limitations described above. For this reason, our group has been investigating the development of PCDs based on polycrystalline silicon (poly-Si) TFTs (Liang *et al* 2016, 2018). Like a-Si:H, poly-Si offers the advantage of allowing fabrication of very large area, monolithic circuits. In addition, poly-Si TFTs exhibit good radiation damage resistance (Li *et al* 2006). Moreover, the mobilities of n-type and p-type poly-Si are ~10^2 and 10^4 times higher than those of a-Si:H, respectively, and within a factor of 10 of those of c-Si—allowing the creation of the type of complex, high-speed circuits required for PCDs.

In this context, it is interesting to examine the possibility of employing PCDs based on poly-Si TFTs for CBCT. In this paper, an investigation is reported for two cases corresponding to imaging applications where improve-

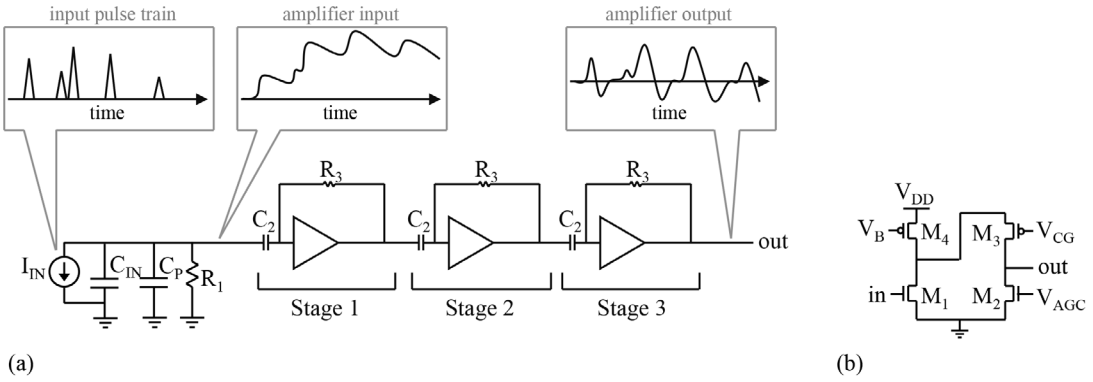

Figure 1. (a) Schematic circuit diagram of the three-stage amplifier design examined in this study. (b) Folded cascode circuit which corresponds to the triangle symbols appearing in the amplifier diagram—consisting of four transistors (M_1, M_2, M_3 and M_4). The values of R_1 and R_3 are 2 MΩ and 15 MΩ, respectively, the values of C_P and C_2 are 100 pF and 500 pF, respectively, and V_{DD} is a power rail set to 8 V. Other symbols in the figure are described in the main text. For purposes of illustrating the response of the circuit to the input pulse train, waveforms at certain points of the signal chain are schematically shown.

Table 1. Summary of input parameters used in the simulations for the BCT and kV-CBCT cases.

Case	Incident spectrum	Mean input x-ray energy	CZT thickness	Pixel pitch	CZT capacitance	Average input flux	Average input flux per pixel
BCT	49 kVp	33 keV	500 μm	330 μm	17.3 pF	1 Mcps mm^{-2}	108.9 kcps/pixel
kV-CBCT	120 kVp	69 keV	1000 μm	400 μm	15.4 pF	450 kcps mm^{-2}	72.0 kcps/pixel

ments in image contrast would be beneficial: CBCT used for breast imaging and kilo-voltage CBCT used for providing localization information in image guided radiotherapy (referred to as BCT and kV-CBCT, respectively). Building upon previous studies in which the capabilities of the various components of poly-Si PCD pixel circuits have been examined (Liang *et al* 2016, 2018), a theoretical study has been performed to investigate whether the amplifier component of poly-Si designs can support the count rates associated with BCT and kV-CBCT imaging. The study, which significantly expands upon and extends the simpler methodology reported in a preliminary examination of this topic (Liang *et al* 2019), includes determination of the energy response profiles and an estimate of energy resolution for that component. In addition, calculational estimates of the number of energy bins that could be provided using poly-Si circuitry for pixel designs consistent with the needs of those imaging applications are reported.

2. Methods

2.1. Amplifier design and input conditions

The schematic circuit diagram of the amplifier design examined in this study for each of the BCT and kV-CBCT cases is shown in figure 1. The design corresponds to a three-stage folded cascode architecture whose development and operation are described in Liang *et al* (2018). The circuit requires three bias voltages (labeled V_{AGC}, V_{CG}, and V_B) to control the gain and settling time of the amplifier. The current source I_{IN} provides signal input to the amplifier. The capacitor C_{IN} corresponds to the capacitance formed by a cadmium zinc telluride (CZT) x-ray converter. The converter was assumed to have a relative permittivity of 10.9 and an effective work function (W_{EFF}) of 4.6 eV (Limousin 2003). The capacitance of C_{IN} varies as a function of pixel pitch (where a fill factor of 100% is assumed) and converter thickness—both of which varied depending on the case.

Table 1 shows various parameter values assumed in the study for each of the two cases. CZT converter thicknesses of 500 and 1000 μm, as well as pixel pitches of 330 and 400 μm (corresponding to the pitches employed in current imagers), were chosen for BCT and kV-CBCT, respectively (Groh *et al* 2002, Sarno *et al* 2015). The combination of converter thickness and pixel area resulted in C_{IN} capacitance values of 17.3 and 15.4 pF for BCT and kV-CBCT, respectively. The input pulses to the amplifier were generated according to distributions that represent the absorbed energy distributions in the CZT converter. These generated distributions, which are referred to as *input spectra*, were obtained with the EGS4 radiation transport code using incident x-ray spectra of the type employed in the two applications. For BCT, the incident spectrum was based on a 49 kVp spectrum (Sechopoulos *et al* 2010) filtered through a 5 cm thick breast with 50/50 adipose and glandular tissue. For kV-CBCT, the incident spectrum was generated using TASMIP (Boone and Seibert 1997) and assumed to be 120 kVp filtered through 40 mm Al resulting in a HVL of 11.5 mm Al—corresponding to an RQA9 spectrum in IEC 61267. Note that the absorption efficiencies of the incident spectra are ~99.5% and 85.5% for the chosen converter thicknesses while

the mean energies for the input spectra are ~33 and 69 keV for BCT and kV-CBCT, respectively. The typical average input flux for the BCT (Cho *et al* 2014) and kV-CBCT (Son *et al* 2017) cases are also given in the table. For a given case, the average input flux per pixel is calculated by multiplying the average input flux by the square of the pixel pitch assumed for that case.

2.2. Determination of optimal operating conditions

The optimal operating conditions of the amplifier refer to the set of bias voltages V_{AGC}, V_{CG}, and V_B that provides the fastest settling time while fulfilling two criteria: (i) an amplifier output response exceeding 1.25 V; and (ii) nonlinearity less than 10%. An energy resolution value (ΔE_{TFT}) that corresponds to the noise produced by the transistors of the circuit is also calculated at these optimal operating conditions. Details of how settling time, nonlinearity and energy resolution are determined are described in Liang *et al* (2018). Note that, in the current study, ΔE_{TFT} is the full-width at half-maximum (FWHM) representation of E_{noise} from that reference (i.e. $\Delta E_{TFT} = E_{noise} \times 2.35$).

The optimal operating conditions for each of the BCT and kV-CBCT cases were determined by simulating the input pulse from a single x-ray photon with an energy corresponding to the mean energy of the associated imaging application (i.e. 33 and 69 keV for BCT and kV-CBCT, respectively). The simulations were performed using the framework described in Liang *et al* (2016) employing the Eldo SPICE circuit simulation software package (Mentor Graphics, OR). The transistors of the amplifier were modeled using version 2 of the RPI poly-Si model (Iniguez *et al* 1999). In order to make the results more representative of the level of performance expected from a modern poly-Si manufacturing process, the parameter values for the RPI model were set to values obtained from empirical characterization of recently-manufactured poly-Si test TFTs. These parameter values correspond to the 'standard transistor' described in Liang *et al* (2016). The optimal operating conditions for each case were used to calculate values for count rate, as described in the next section.

2.3. Determination of count rates and energy response profiles

Count rate performance was determined using the methodology of Liang *et al* (2018), briefly summarized as follows. Input pulses, generated by using the W_{EFF} of CZT to convert the energy deposited by each x-ray into a current pulse, are presented to the amplifier, simulations determine the response of that circuit, and the output response of the amplifier is analyzed to evaluate performance. The input pulses have a rise time of 20 ns and a fall time of 80 ns, resulting in a pulse width of 100 ns (Fink *et al* 2006). The input pulses are grouped into sets of 10 000 pulses, referred to as an input pulse train. For a given case (BCT or kV-CBCT), the pulse height distribution of a given pulse train corresponds to the input spectrum assumed for that case. The total time duration of the pulse train is varied in order to simulate different input fluxes. The input pulses are randomly spaced in time within that duration in order to simulate the stochastic nature of x-ray events. The output response of the amplifier was analyzed by applying a threshold to the output waveform and counting the number of times that threshold was exceeded.

In the study, the input pulse train duration ranged from 10 s to 1 ms—corresponding to input fluxes (expressed in units of counts per second, cps) ranging from 1 kcps to 10 Mcps. The threshold was set to 10 keV in order to count as many input photons as possible, since neither the BCT nor the kV-CBCT input spectrum provided x-ray photons below that energy. For each input flux, the number of times the output waveform exceeded that threshold was recorded. The count rate of the amplifier is the number of counts recorded divided by the pulse train duration. As input flux increases, the count rate will not increase proportionally due to pulse pile-up, also known as dead time loss. In this study, results are reported for 10% dead time loss.

This same simulation framework was also used to determine energy response profiles (Liang *et al* 2018). Energy response profiles were created by varying the threshold applied to the output of the amplifier from 0.5 to 199.5 keV in 1 keV steps, and tallying the number of counts that fall between consecutive threshold values. The histogram of the results is the energy response profile. The energy response profile of the circuit in response to an input spectrum (i.e. 49 kVp or 120 kVp) illustrates the degree of distortion of the input spectrum as a function of input flux. The energy response profile in response to a monoenergetic input was used to characterize the energy resolution of the amplifier as a function of input flux (ΔE_{FLUX}) for each of the cases. ΔE_{FLUX} is given by the FWHM value of the energy response profile.

2.4. Estimation of number of energy thresholds

Compared to minimum feature sizes on the order of tens to hundreds of nanometers for c-Si (which have allowed development of PCDs with numerous energy thresholds at pixel sizes well below 100 μm), it has been estimated that a minimum feature size of 1 μm would allow a minimum pixel size of 243 μm for poly-Si photon counting pixel circuits equipped with a single energy threshold and a 9-bit counter (Liang *et al* 2016). Since the pixel pitches assumed for the BCT and kV-CBCT cases in this study were 330 and 400 μm, respectively, an analytical calculation was performed to estimate the number of energy thresholds a pixel could provide for each case. The

Table 2. Optimal operating conditions and circuit characteristics for each of the BCT and kV-CBCT cases. See text for further details.

Case	V_{AGC}	V_{CG}	V_B	Output response	Nonlinearity	Settling time	ΔE_{TFT}
BCT	2.7 V	3.5 V	3.25 V	1.65 V	9.8%	5.5 μs	2.1 keV
kV-CBCT	3.3 V	3.0 V	2.0 V	2.63 V	5.4%	3.6 μs	2.2 keV

calculations, which assumed the same 15-bit counter commonly reported in other clinical and prototype photon counting devices (Amendolia *et al* 1999), were performed using the same methodology of that previous study.

To estimate the minimum pixel pitch required for a given pixel circuit design, the circuit area occupied by each of the four pixel circuit components (i.e. the amplifier, comparator, clock generator, and counter) of a poly-Si photon counting detector was first calculated. The circuit area for a given component was calculated by summing the area occupied by circuit elements (i.e. resistors, transistors, or capacitors) along with estimates of the margins around each component. The sum of the areas of all four components, plus an additional factor to account for wires needed for signal routing, is the total circuit area for the pixel circuit. The square-root of that total area is the estimated minimum pixel pitch.

Each additional threshold in the pixel circuit beyond the first requires another set of comparator, clock generator, and counter components. Additional circuitry was introduced into the calculation until the point where further additions would exceed the available circuit area for a given case.

3. Results

3.1. Optimal operating conditions and circuit characteristics

The optimal operating conditions of the amplifier for each of the BCT and kV-CBCT cases are shown in table 2. In addition, values for output response, degree of nonlinearity, settling time, and energy resolution are also shown. The kV-CBCT case exhibits better nonlinearity and settling time, primarily due to higher energy x-ray photons that produce larger input signal. Due to this larger signal, the amplifier does not need to provide as much gain—which results in better linearity and allows for a better selection of optimal operating conditions that provide faster settling time.

3.2. Count rate, energy response profiles and energy resolution

For each of the BCT and kV-CBCT cases, count rate simulations were performed at the optimal operating conditions. The count rate results are shown in figure 2. The input flux values were chosen to be roughly distributed evenly across log-space, except for the region where 10% dead time loss occurs. This finer simulation density allowed for more precise interpolation in order to find the count rate at 10% dead time loss. Both cases exhibit largely linear behavior up to ~100 kcps. The kV-CBCT case has higher count rate—due to the faster settling time of the circuit. The count rate at 10% dead time loss is 225 kcps/pixel for BCT and 270 kcps/pixel for kV-CBCT. These count rates are two and four times higher than the average input fluxes given in table 1 for BCT and kV-CBCT, respectively.

The energy response profiles for each case in response to the input spectra as a function of input flux are shown in figure 3. When input flux is low (10 kcps/pixel) and both cases exhibit almost no dead time loss (<0.1%), the output response is nearly identical to the input spectrum. When the input flux is 250 kcps/pixel (where both cases exhibit ~10% dead time loss), the output response is still a good representation of the input spectrum. In particular, the output response for the kV-CBCT case still exhibits the K-edge peaks of the input spectrum. When the input flux is 800 kcps/pixel and the kV-CBCT case has ~25% dead time loss, those K-edge peaks are absent in the output response. As input flux increases further to 2000 kcps/pixel, where both cases exhibit greater than 50% dead time loss, the output response and input spectrum differ greatly.

Energy response profiles in response to a monoenergetic x-ray input are shown in figure 4. At 10 kcps/pixel (corresponding to a dead time loss of nearly zero), the FWHM of the profile is limited by the binning resolution chosen for the simulations (i.e. 1 keV). As input flux increases, the output response profile widens, resulting in increasing FWHM values—so that, for example, at an input flux of 250 kcps/pixel, the FWHM is ~1.4 keV for BCT and 1.8 keV for kV-CBCT. Note that the low energy tails observed in some of the profiles are the result of undershoot of the amplifier output response (Liang *et al* 2018), and are not a result of charge sharing. While the simulations of the individual pixel circuits performed in this study do not account for charge sharing, this effect is not expected to greatly affect the performance of 330 and 400 μm pitch pixels since lateral diffusion of charge in CZT at diagnostic x-ray energies is on the order of 100 to 200 μm (Seller *et al* 2011).

A summary of the count rate and energy resolution performance of both cases is shown in table 3. Since the noise generated by TFTs and the noise due to input flux are assumed to be independent, the two noise values were combined by summing in quadrature to produce ΔE_{sum}. The ΔE_{sum} value divided by the mean x-ray energy of each spectrum gives an energy resolution metric. The combined energy resolution is 7.6% for BCT and 4.3% for

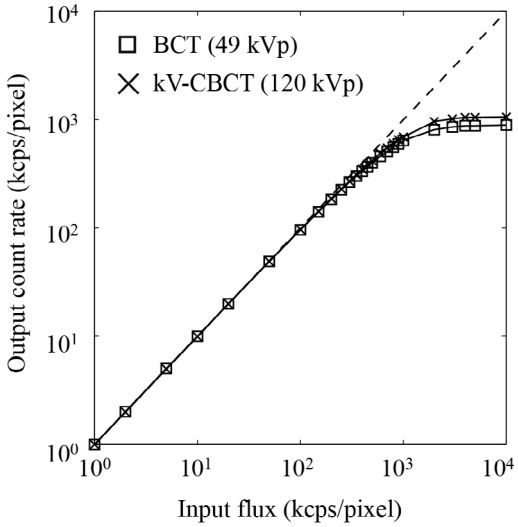

Figure 2. Output count rate as a function of varying input flux for each of the BCT and kV-CBCT cases. In each case, a solid line is drawn to connect the points to guide the eye. The dashed line indicates a one-to-one correspondence between input flux and output count rate.

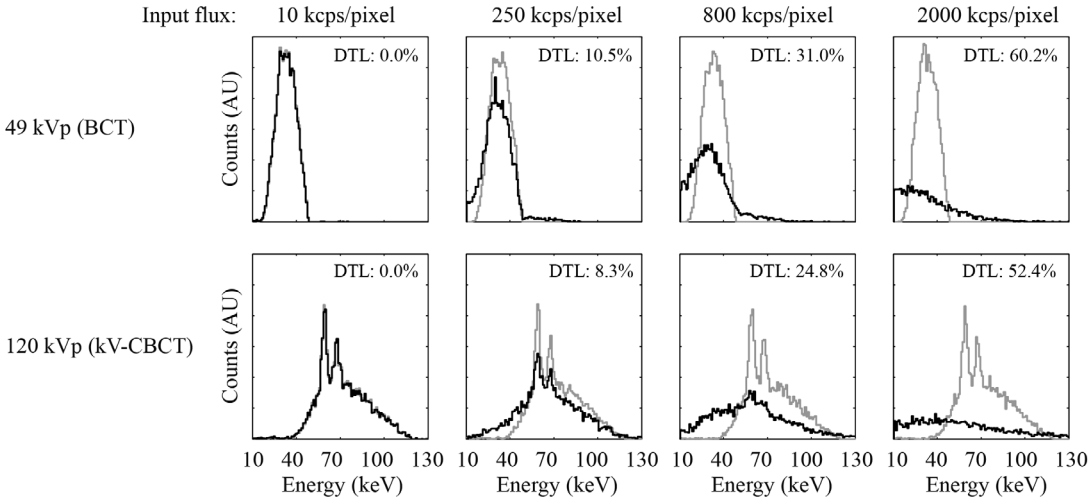

Figure 3. Energy response profiles of the amplifier circuit in response to the input spectrum associated with each of the BCT and kV-CBCT cases. Results are shown as a function of input flux. In each plot, the grey and black curves represent the input spectrum and the corresponding output response, respectively. The dead time loss (DTL) at each input flux for each case is also given.

kV-CBCT. By comparison, energy resolution values of 10% to 15% have been reported for the full circuit of c-Si photon counting devices (Barber *et al* 2009, Fredenberg *et al* 2010).

3.3. Number of energy thresholds

The maximum number of energy thresholds that can be implemented in the pixel area assumed for each of the BCT and kV-CBCT cases is shown in figure 5. For purposes of comparison, the estimated area of a previously investigated, poly-Si, photon counting pixel circuit (referred to as SPC1) is also shown (Liang *et al* 2016). The 15-bit counter assumed in the present study occupies more circuit area than the 9-bit counter of SPC1. For BCT, circuitry for two energy thresholds would fit within the area of the assumed 330 μm pitch pixel, and occupy 89.7% of the area. For kV-CBCT, circuitry for three energy thresholds would fit within the area of the assumed 400 μm pitch pixel, and occupy 81.7% of the area. In the event that charge sharing was determined to reduce performance, an interesting possibility would be to use the unoccupied pixel area to incorporate anti-coincidence logic (Ballabriga *et al* 2011, Hsieh and Sjolin 2018) to detect if the energy of one x-ray photon is deposited in multiple pixels.

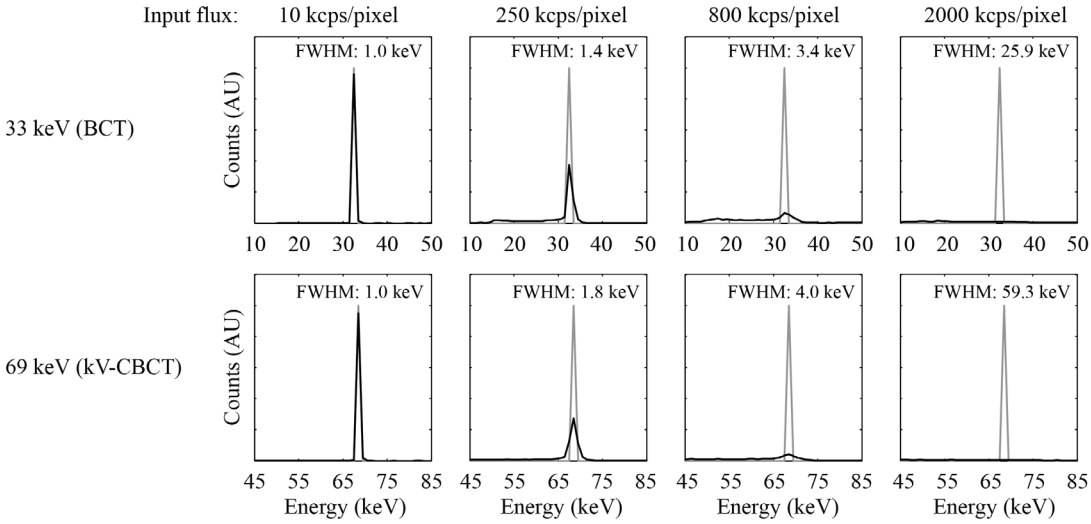

Figure 4. Energy response profiles of the amplifier circuit in response to monoenergetic input spectrum associated with each of the BCT and kV-CBCT cases. Conventions for the data shown and what the profiles represent are the same as for figure 3. The FWHM value for the output response at each input flux for each case is also given.

Table 3. Count rate and energy resolution results for each of the BCT and kV-CBCT cases. Note that ΔE_{TFT}, the energy resolution value associated with the TFTs in the circuit, depends on the optimal operating conditions for each case, but is independent of input flux and output count rate.

Case	Count rate (10% dead time loss)	ΔE_{TFT}	ΔE_{FLUX}	ΔE_{sum}	Mean input x-ray energy	Energy resolution
BCT	225 kcps	2.1 keV	1.4 keV	2.5 keV	33 keV	7.6%
kV-CBCT	270 kcps	2.2 keV	2.0 keV	3.0 keV	69 keV	4.3%

4. Discussion

The performance of hypothetical poly-Si amplifier circuit designs, configured for photon counting for the cases of BCT and kV-CBCT, has been evaluated. Circuit simulations were used to produce results as a function of several application-specific parameters, such as input spectrum, pixel pitch and converter thickness. From these results, a number of interesting observations can be made.

The energy resolution capabilities of the amplifier designs were estimated by independently simulating the noise generated by each transistor in the amplifier circuit, as well as simulating the effect of pulse pile-up. The simulations predict that the designs would exhibit energy resolutions of 7.6% and 4.3% for BCT and kV-CBCT, respectively. While these are well below the 10% to 15% values reported for c-Si photon counting devices, more meaningful comparisons would require that the full poly-Si pixel circuit (i.e. the amplifier, comparator, clock generator and counter) be modeled. In addition, future modeling should also account for the thermal noise of the transistors as well as the thermal and flicker noise of the resistors.

The output count rates of the amplifier designs were found to be two and four times higher than the average flux for the BCT and kV-CBCT cases, respectively. While this is encouraging, it should be noted that the instantaneous flux for BCT and kV-CBCT can be much higher than the average fluxes considered in this study—given the stochastic nature of the x-ray photons emitted by an actual source. For that reason, photon counting pixel circuits are typically designed to provide count rates much higher than the average flux (Taguchi and Iwanczyk 2013)—for example, by a factor of 10. An amplifier circuit with a count rate capability 10 times higher than the input flux will exhibit less pulse pile-up, which could also improve energy resolution. Given that the amplifier designs examined in this investigation are based on an amplifier circuit identified in a previous study, it is likely that designs exhibiting performance superior to that reported in the present study could be identified through further circuit simulations. For example, future simulations could explore circuit architectures other than the folded cascode architecture considered in the present study.

Finally, the present investigation suggests that, under the assumptions of the study, circuitry for multiple energy thresholds could be included in the pixels for each of the BCT and kV-CBCT cases. In this context, it is interesting to note that the pixel pitch chosen for kV-CBCT is almost large enough to include an additional (fourth) energy threshold—but would occupy 102% of the total pixel area. A potential optimization that would allow a fourth threshold without changing the pixel pitch would be to decrease the circuit area of capacitors by

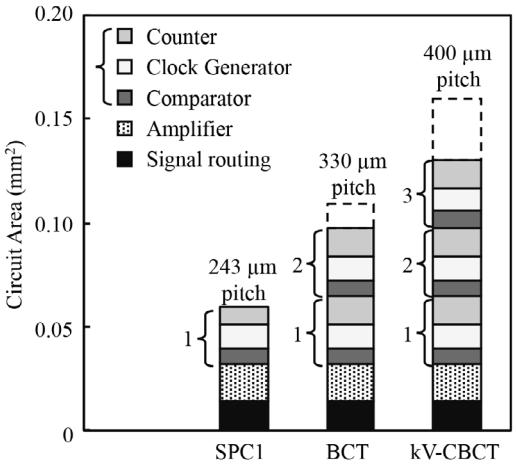

Figure 5. Illustration of the estimated area of pixel circuit components that could be incorporated into individual pixels for the BCT and kV-CBCT cases. The dashed boxes correspond to the areas of the 330 μm and 400 μm pitch pixels assumed for the BCT and kV-CBCT cases, respectively. For each case, the areas required for the amplifier and signal routing, along with the areas required for the components needed to implement a threshold (one comparator, clock generator and counter per threshold) are shown by shaded regions. Each bracket delineates the components for a single threshold. See text for further details.

either decreasing the thickness of the SiO_2 dielectric material, or replacing the SiO_2 dielectric material with a material that provides a higher dielectric constant (also referred to as a high-κ material), such as hafnium dioxide (HfO_2) (Beckx *et al* 2005, Lin *et al* 2006) or zirconium dioxide (ZrO_2) (Copel *et al* 2000). Since capacitors occupy the majority of the circuit area for the amplifier component and, as is evident in figure 5, the amplifier occupies a relatively large fraction of the total pixel circuit area, this optimization could have a non-negligible impact on reducing the total area needed for the circuit. For example, employing HfO_2 or ZrO_2 (Robertson 2004) would decrease the circuit area of the amplifier component by 58%—resulting in a four-threshold design that occupies 96% of the available area of a 400 μm pitch pixel. The other three pixel circuit components employ much smaller capacitors or employ no capacitors and would therefore benefit minimally from the use of such strategies.

The choice of CZT for this study follows from the widespread use of this converter material in c-Si PCDs (Iniewski 2014)—a result of its high effective atomic number (~50), high density (5.8 g cm^{-3}), favorable band-gap (1.4 to 2.2 eV) and room temperature operation (Diéguez 2011). The challenge of producing CZT in large areas and with few defects is widely recognized and a variety of efforts have been reported to overcome these obstacles (Roy *et al* 2009, Yang *et al* 2013, Zhou *et al* 2018).

The simulation results of the present study support the hypothesis that poly-Si-based amplifiers can perform sufficiently well to enable photon counting for the BCT and kV-CBCT imaging applications. Motivated by the encouraging results of this study, it would be sensible to conduct a detailed examination of the performance of the other components of the photon counting pixel circuits—such as of the count rate and energy resolution of the next crucial circuit element, the comparator component. These investigations are planned in parallel with empirical measurements of our first generation of poly-Si photon counting circuits. Such studies are expected to provide further insight as to how to achieve pixel circuit designs optimized for large area, monolithic detectors suitable for BCT and kV-CBCT.

Acknowledgments

The authors would like to thank John McDonald and Mike Yeakey for technical support in the maintenance of the computational cluster used to perform the simulations in this study.

References

Abuhaimed A, Martin C J and Sankaralingam M 2018 A Monte Carlo study of organ and effective doses of cone beam computed tomography (CBCT) scans in radiotherapy *J. Radiol. Prot.* **38** 61–80

Amendolia S R *et al* 1999 MEDIPIX: a VLSI chip for a GaAs pixel detector for digital radiology *Nucl. Instrum. Methods Phys. Res.* A **422** 201–5

Antonuk L E, El-Mohri Y, Hall A, Jee K-W, Maolinbay M, Nassif S C, Rong X, Siewerdsen J H, Zhao Q and Weisfield R L 1998 A large-area, 97 μm pitch, indirect-detection, active matrix, flat-panel imager (AMFPI) *Proc. SPIE* **3336** 2–13

Antonuk L E, Jee K-W, El-Mohri Y, Maolinbay M, Nassif S, Rong X, Zhao Q, Siewerdsen J H, Street R A and Shah K S 2000 Strategies to improve the signal and noise performance of active matrix, flat-panel imagers for diagnostic x-ray applications *Med. Phys.* **27** 289–306

Ballabriga R, Campbell M, Heijne E, Llopart X, Tlustos L and Wong W 2011 Medipix3: A 64 k pixel detector readout chip working in single photon counting mode with improved spectrometric performance *Nucl. Instrum. Methods Phys. Res.* A **633** S15–8

Barber W C *et al* 2009 Characterization of a novel photon counting detector for clinical CT: count rate, energy resolution, and noise performance *Proc. SPIE* **7258** 725824
Beckx S, Demand M, Locorotondo S, Henson K, Claes M, Paraschiv V, Shamiryan D, Jaenen P, Boullart W and Degendt S 2005 Implementation of high-k and metal gate materials for the 45 nm node and beyond: gate patterning development *Microel. Reliab.* **45** 1007–11
Boone J and Seibert J 1997 An accurate method for computer-generating tungsten anode x-ray spectra from 30 to 140 kV *Med. Phys.* **24** 1661–70
Boone J M, Nelson T R, Lindfors K K and Seibert J A 2001 Dedicated breast CT: radiation dose and image quality evaluation *Radiology* **221** 657–67
Campbell M, Heijne E, Meddeler G, Pernigotti E and Snoeys W 1998 A readout chip for a 64 × 64 pixel matrix with 15-bit single photon counting *IEEE Trans. Nucl. Sci.* **45** 751–3
Cao Q, Sisniega A, Brehler M, Stayman J W, Yorkston J, Siewerdsen J H and Zbijewski W 2018 Modeling and evaluation of a high-resolution CMOS detector for cone-beam CT of the extremities *Med. Phys.* **45** 114–30
Cho H-M, Barber W C, Ding H, Iwanczyk J S and Molloi S 2014 Characteristic performance evaluation of a photon counting Si strip detector for low dose spectral breast CT imaging *Med. Phys.* **41** 091903
Copel M, Gribelyuk M and Gusev E 2000 Structure and stability of ultrathin zirconium oxide layers on Si (0 0 1) *Appl. Phys. Lett.* **76** 436–8
Diéguez E 2011 *Comprehensive Semiconductor Science and Technology* ed P Bhattacharya *et al* (Amsterdam: Elsevier) pp 170–201
Fink J, Kruger H, Lodomez P and Wermes N 2006 Characterization of charge collection in CdTe and CZT using the transient current technique *Nucl. Instrum. Methods Phys. Res.* A 435–43
Fischer P, Helmich A, Lindner M, Wermes N and Blanquart L 2000 A photon counting pixel chip with energy windowing *IEEE Trans. Nucl. Sci.* **47** 881–4
Fredenberg E, Lundqvist M, Aslund M, Hemmendorff M, Cederstrom B and Danielsson M 2009 A photon-counting detector for dual-energy breast tomosynthesis *Proc. SPIE* **7258** 72581J
Fredenberg E, Lundqvist M, Cederstrom B, Aslund M and Danielsson M 2010 Energy resolution of a photon-counting silicon strip detector *Nucl. Instrum. Methods Phys. Res.* A **613** 156–62
Gazi P M, Yang K, Burkett G W Jr, Aminololama-Shakeri S, Seibert J A and Boone J M 2015 Evolution of spatial resolution in breast CT at UC Davis *Med. Phys.* **42** 1973–81
Groh B A, Siewerdsen J H, Drake D G, Wong J W and Jaffray D A 2002 A performance comparison of flat-panel imager-based MV and kV cone-beam CT *Med. Phys.* **29** 967–75
Guerrero M E, Jacobs R, Loubele M, Schutyser F, Suetens P and van Steenberghe D 2006 State-of-the-art on cone beam CT imaging for preoperative planning of implant placement *Clin. Oral Investig.* **10** 1–7
Gutjahr R, Halaweish A, Yu Z, Leng S, Yu L, Li Z, Jorgensen S, Ritman E, Kappler S and McCollough C 2016 Human imaging with photon-counting-based CT at clinical dose levels: contrast-to-noise ratio and cadaver studies *Investig. Radiol.* **51** 421
Hodez C, Griffaton-Taillandier C and Bensimon I 2011 Cone-beam imaging: applications in ENT *Eur. Ann. Otorhinolaryngol. Head Neck Dis.* **128** 65–78
Hsieh S S and Sjolin M 2018 Digital count summing versus analog charge summing for photon counting detectors: a performance simulation study *Med. Phys.* **45** 4085–93
Iniewski K 2014 CZT detector technology for medical imaging *J. Instrum.* **9** C11001
Iniguez B, Xu Z, Fjeldly T A and Shur M S 1999 Unified model for short-channel poly-Si TFTs *Solid-State Electron.* **43** 1821–31
Jaffray D A, Siewerdsen J H, Wong J W and Martinez A A 2002 Flat-panel cone-beam computed tomography for image-guided radiation therapy *Int. J. Radiat. Oncol. Biol. Phys.* **53** 1337–49
Jiang H, Zhao Q, Antonuk L E, El-Mohri Y and Gupta T 2013 Development of active matrix flat panel imagers incorporating thin layers of polycrystalline HgI_2 for mammographic x-ray imaging *Phys. Med. Biol.* **58** 703–14
Job I, Ganguly A, Vernekohl D, Weisfield R, Muñoz E, Zhang J, Tognina C and Colbeth R 2019 Comparison of CMOS and amorphous silicon detectors: determining the correct selection criteria, to optimize system performance for typical imaging tasks *Proc. SPIE* **10948** 109480F
Koniczek M, Antonuk L E, El-Mohri Y, Liang A K and Zhao Q 2017 Theoretical investigation of the noise performance of active pixel imaging arrays based on polycrystalline silicon thin film transistors *Med. Phys.* **44** 3491–503
Li Y, Antonuk L E, El-Mohri Y, Zhao Q, Du H, Sawant A and Wang Y 2006 Effects of x-ray irradiation on polycrystalline silicon, thin-film transistors *J. Appl. Phys.* **99** 064501
Liang A K, El-Mohri Y, Zhao Q, Koniczek M and Antonuk L E 2019 Theoretical count rate capabilities of polycrystalline silicon photon counting imagers for CBCT applications *Proc. SPIE* **10948** 1094819
Liang A K, Koniczek M, Antonuk L E, El-Mohri Y and Zhao Q 2018 Theoretical investigation of the count rate capabilities of in-pixel amplifiers for photon counting arrays based on polycrystalline silicon TFTs *Med. Phys.* **45** 4418–29
Liang A K, Koniczek M, Antonuk L E, El-Mohri Y, Zhao Q, Street R A and Lu J P 2016 Performance of in-pixel circuits for photon counting arrays (PCAs) based on polycrystalline silicon TFTs *Phys. Med. Biol.* **61** 1968–85
Limousin O 2003 New trends in CdTe and CdZnTe detectors for X- and gamma-ray applications *Nucl. Instrum. Methods Phys. Res.* A **504** 24–37
Lin C-P, Tsui B-Y, Yang M-J, Huang R-H and Chien C-H 2006 High-performance poly-silicon TFTs using HfO_2 gate dielectric *IEEE Electron Device Lett.* **27** 360–3
Llopart X, Campbell M, Dinapoli R, San Segundo D and Pernigotti E 2002 Medipix2: a 64 k pixel readout chip with 55 μm square elements working in single photon counting mode *IEEE Trans. Nucl. Sci.* **49** 2279–83
Oh K, Shin J and Kim S 2012 The development of efficient x-ray conversion material for digital mammography *J. Instrum.* **7** C02009
Pourmorteza A, Symons R, Reich D, Bagheri M, Cork T, Kappler S, Ulzheimer S and Bluemke D 2017 Photon-counting CT of the brain: *in vivo* human results and image-quality assessment *Am. J. Neuroradiol.* **38** 2257–63
Pourmorteza A, Symons R, Sandfort V, Mallek M, Fuld M, Henderson G, Jones E, Malayeri A, Folio L and Bluemke D 2016 Abdominal imaging with contrast-enhanced photon-counting CT: first human experience *Radiology* **279** 239–45
Robertson J 2004 High dielectric constant oxides *Eur. Phys. J.: Appl. Phys.* **28** 265–91
Roessl E and Proksa R 2007 K-edge imaging in x-ray computed tomography using multi-bin photon counting detectors *Phys. Med. Biol.* **52** 4679–96
Roy U N, Gueorguiev A, Weiller S and Stein J 2009 Growth of spectroscopic grade $Cd_{0.9}Zn_{0.1}Te$:In by THM technique *J. Cryst. Growth* **312** 33–6
Rumboldt Z, Huda W and All J W 2009 Review of portable CT with assessment of a dedicated head CT scanner *AJNR Am. J. Neuroradiol.* **30** 1630–6

Sarno A, Mettivier G and Russo P 2015 Dedicated breast computed tomography: basic aspects *Med. Phys.* **42** 2786–804
Scheuermann J R, Goldan A H, Tousignant O, Leveille S and Zhao W 2015 Development of solid-state avalanche amorphous selenium for medical imaging *Med. Phys.* **42** 1223–6
Sechopoulos I, Feng S S and D'Orsi C J 2010 Dosimetric characterization of a dedicated breast computed tomography clinical prototype *Med. Phys.* **37** 4110–20
Segui J A and Zhao W 2006 Amorphous selenium flat panel detectors for digital mammography: validation of a NPWE model observer with CDMAM observer performance experiments *Med. Phys.* **33** 3711–22
Seller P *et al* 2011 Pixellated Cd(Zn)Te high-energy x-ray instrument *J. Instrum.* **6** C12009
Shen Y, Zhong Y, Lai C J, Wang T and Shaw C C 2013 Cone beam breast CT with a high pitch (75 μm), thick (500 μm) scintillator CMOS flat panel detector: visibility of simulated microcalcifications *Med. Phys.* **40** 101915
Shikhaliev P M and Fritz S G 2011 Photon counting spectral CT versus conventional CT: comparative evaluation for breast imaging application *Phys. Med. Biol.* **56** 1905–30
Son K, Kim J S, Lee H and Cho S 2017 Imaging dose of human organs from kV-CBCT in image-guided radiation therapy *Radiat. Prot. Dosimetry* **175** 194–200
Street R A, Nelson S, Antonuk L and Perez Mendez V 1990 Amorphous silicon sensor arrays for radiation imaging *Mater. Res. Soc. Symp. Proc.* vol **192** pp 441–52
Street R A, Ready S E, van Schuylenbergh K, Ho J, Boyce J B, Nylen P, Shah K, Melekhov L and Hermon H 2002 Comparison of PbI_2 and HgI_2 for direct detection active matrix x-ray image sensors *J. Appl. Phys.* **91** 3345–55
Symons R, Reich D, Bagheri M, Cork T, Krauss B, Ulzheimer S, Kappler S, Bluemke D and Pourmorteza A 2018 Photon-counting computed tomography for vascular imaging of the head and neck: first *in vivo* human results *Investig. Radiol.* **53** 135–42
Taguchi K and Iwanczyk J S 2013 Vision 20/20: single photon counting x-ray detectors in medical imaging *Med. Phys.* **40** 100901
Tanguay J, Yun S, Kim H K and Cunningham I A 2015 Detective quantum efficiency of photon-counting x-ray detectors *Med. Phys.* **42** 491–509
Yang G *et al* 2013 Post-growth thermal annealing study of CdZnTe for developing room-temperature x-ray and gamma-ray detectors *J. Cryst. Growth* **379** 16–20
Zbijewski W *et al* 2011 A dedicated cone-beam CT system for musculoskeletal extremities imaging: design, optimization, and initial performance characterization *Med. Phys.* **38** 4700–13
Zhao W, Li D, Reznik A, Lui B J, Hunt D C, Rowlands J A, Ohkawa Y and Tanioka K 2005 Indirect flat-panel detector with avalanche gain: fundamental feasibility investigation for SHARP-AMFPI (scintillator HARP active matrix flat panel imager) *Med. Phys.* **32** 2954–66
Zhao W and Rowlands J A 1995 X-ray imaging using amorphous selenium: Feasibility of a flat-panel self-scanned detector for digital radiology *Med. Phys.* **22** 1595–604
Zhou B, Jie W, Wang T, Xu Y, Yang F, Yin L, Zhang B and Nan R 2018 Growth and characterization of detector-grade $Cd_{0.9}Zn_{0.1}Te$ crystals by the traveling heater method with the accelerated crucible rotation technique *J. Electron. Mater.* **27** 1125–30